EMERGING COMPUTING

Reconfigurable perovskite nickelate electronics for artificial intelligence

Hai-Tian Zhang[1*†‡], Tae Joon Park[1*†], A. N. M. Nafiul Islam[2†], Dat S. J. Tran[3†], Sukriti Manna[4,5†], Qi Wang[1†], Sandip Mondal[1§], Haoming Yu[1], Suvo Banik[4,5], Shaobo Cheng[6¶], Hua Zhou[7], Sampath Gamage[8], Sayantan Mahapatra[9], Yimei Zhu[6], Yohannes Abate[8], Nan Jiang[9], Subramanian K. R. S. Sankaranarayanan[4,5], Abhronil Sengupta[2], Christof Teuscher[10], Shriram Ramanathan[1*]

Reconfigurable devices offer the ability to program electronic circuits on demand. In this work, we demonstrated on-demand creation of artificial neurons, synapses, and memory capacitors in post-fabricated perovskite $NdNiO_3$ devices that can be simply reconfigured for a specific purpose by single-shot electric pulses. The sensitivity of electronic properties of perovskite nickelates to the local distribution of hydrogen ions enabled these results. With experimental data from our memory capacitors, simulation results of a reservoir computing framework showed excellent performance for tasks such as digit recognition and classification of electrocardiogram heartbeat activity. Using our reconfigurable artificial neurons and synapses, simulated dynamic networks outperformed static networks for incremental learning scenarios. The ability to fashion the building blocks of brain-inspired computers on demand opens up new directions in adaptive networks.

Continual learning in artificial intelligence (AI) presents a formidable challenge. Models are generally trained on stationary data distributions, and thus when new data are presented incrementally to a neural network, this interferes with the previously learned knowledge, resulting in poor performance, which is known as catastrophic forgetting and remains an active field of research (*1*, *2*). One of the major approaches to tackle this issue is to actively adapt the structure of the network itself when new data becomes available. Not only does modulating the architecture of the network in response to the input distribution allow the network to manage its resources efficiently, recent discoveries also suggest that a dynamic network can show better performance as compared with that of a static network when provided with equal resources (*3*, *4*). Moreover, as smart edge devices become more integrated into society, they will require the implementation of sophisticated networks in hardware constrained by both chip area and power. Having the ability to reallocate network resources dynamically to perform various tasks in an ever-changing environment will be of fundamental importance (*3*). Having programmable capabilities in hardware can be game changing for future computers whose designs are inspired by the intelligence of animal brains.

In this work, we showed that perovskite nickelates, a class of quantum materials that undergo room-temperature electronic phase transitions upon hydrogen doping, enable a versatile, reconfigurable hardware platform for adaptive computing. A single device made from H-doped $NdNiO_3$ (NNO), for example, could be electrically reconfigured on demand to take on the functionalities of either neurons, synapses, or memory capacitors (Fig. 1A). Such versatile tunability was distinctively enabled by the synergistic combination of a vast array of metastable configurations for protons in the perovskite lattice that can also be voltage controlled. Although a variety of ionic-electronic switches are being explored for neuromorphic computing (*5*–*10*), complete reconfiguration of neuromorphic functions has remained elusive. To demonstrate example applications in AI, we used the experimental data from our memory capacitors in a reservoir computing (RC) framework (Fig. 1B), a brain-inspired machine learning architecture, and simulation results demonstrated excellent performance comparable with those of theoretical and experimental reservoirs. The experimental characteristics of neurons and synapses obtained from the perovskite nickelate devices and their run-time reconfigurability were leveraged to design self-adaptive dynamic grow-when-required (GWR) networks (Fig. 1C). Motivated by the cortical data processing in the brain, GWR networks present an unsupervised approach to lifelong learning in real-world scenarios with limited availability of training samples, which in turn may have missing or noisy labels. We demonstrated that such networks can exploit the creation and deletion of network nodes on the fly to offer greater representation power and efficiency in comparison with those of static counterparts.

Results and discussion

Perovskite nickelates (chemical formula $ReNiO_3$, where Re is a rare-earth ion such as Nd) are a class of quantum materials whose electronic properties are mediated by strong electron interactions. Pristine NNO is a correlated metal at room temperature. Hydrogen dopants as electron donors can lead to a reduction in electrical conductivity by several orders of magnitude through modifying the Ni orbital configuration (*11*). Gently redistributing the hydrogen ions (protons) already doped in the lattice by electric fields can modify the electrical conductivity systematically to generate a multitude of electronic states. For example, by annealing NNO devices in hydrogen gas (with catalytic electrodes such as Pd or Pt), hydrogen can be doped interstitially into the NNO lattice proximal to the electrode. The hydrogen atoms then donate electrons to the Ni *d* orbitals, which changes the filling state in the NNO *d* band and results in a phase transition with a change in resistivity several orders of magnitude. (From here on, the hydrogen-doped NNO will be referred as H-NNO for simplicity.) A vast array of metastable energy states are available to the protons in the lattice, and thus, their distribution and local concentration (and therefore function) can be subsequently modulated with electric fields applied to the electrode. The switching mechanism of the H-NNO device is compared with traditional nonfilamentary resistive memory devices in table S1.

To demonstrate reproducible electrical reconfiguration in H-NNO, 50-nm-thick NNO films were deposited through different methods, sputtering and atomic layer deposition (ALD), as well as on different substrates, $LaAlO_3$ and SiO_2 on Si (structural characterizations of representative pristine NNO films are provided in fig. S3, and device details are provided in fig. S4). First, we described the capacitive behavior (charge storage) in our devices. Capacitors not only are useful for storing charge in the conventional sense but are also central for numerous brain-inspired computing architectures. Evolution of mem-capacitive loop states in the perovskite nickelate device as a function of hydrogen doping is shown in fig. S5. With increasing hydrogen doping, the H-NNO film resistance increased

[1]School of Materials Engineering, Purdue University, West Lafayette, IN 47907, USA. [2]Department of Electrical Engineering, Pennsylvania State University, University Park, PA, 16802, USA. [3]Department of Electrical and Computer Engineering, Santa Clara University, Santa Clara, CA 95053, USA. [4]Center for Nanoscale Materials, Argonne National Laboratory, Argonne, IL 60439, USA. [5]Department of Mechanical and Industrial Engineering, University of Illinois Chicago, Chicago, IL 60607, USA. [6]Department of Condensed Matter Physics and Materials Science, Brookhaven National Laboratory, Upton, NY 11973, USA. [7]X-ray Science Division, Advanced Photon Source, Argonne National Laboratory, Lemont, IL 60439, USA. [8]Department of Physics and Astronomy, University of Georgia, Athens, GA 30602, USA. [9]Department of Chemistry, University of Illinois Chicago, Chicago, IL 60607, USA. [10]Department of Electrical and Computer Engineering, Portland State University, Portland, OR 97201, USA.
***Corresponding author. Email: htzhang@buaa.edu.cn (H.-T.Z.); park1080@purdue.edu (T.J.P.); shriram@purdue.edu (S.R.)**
†These authors contributed equally to this work.
‡Present address: School of Materials Science and Engineering, Beihang University, Beijing 100191, China.
§Present address: Department of Electrical Engineering, Indian Institute of Technology Bombay, Mumbai 400076, India.
¶Present address: Key Laboratory of Material Physics, School of Physics and Microelectronics, Zhengzhou University, Zhengzhou 450052, China.

Downloaded from https://www.science.org at University of Georgia on February 06, 2022

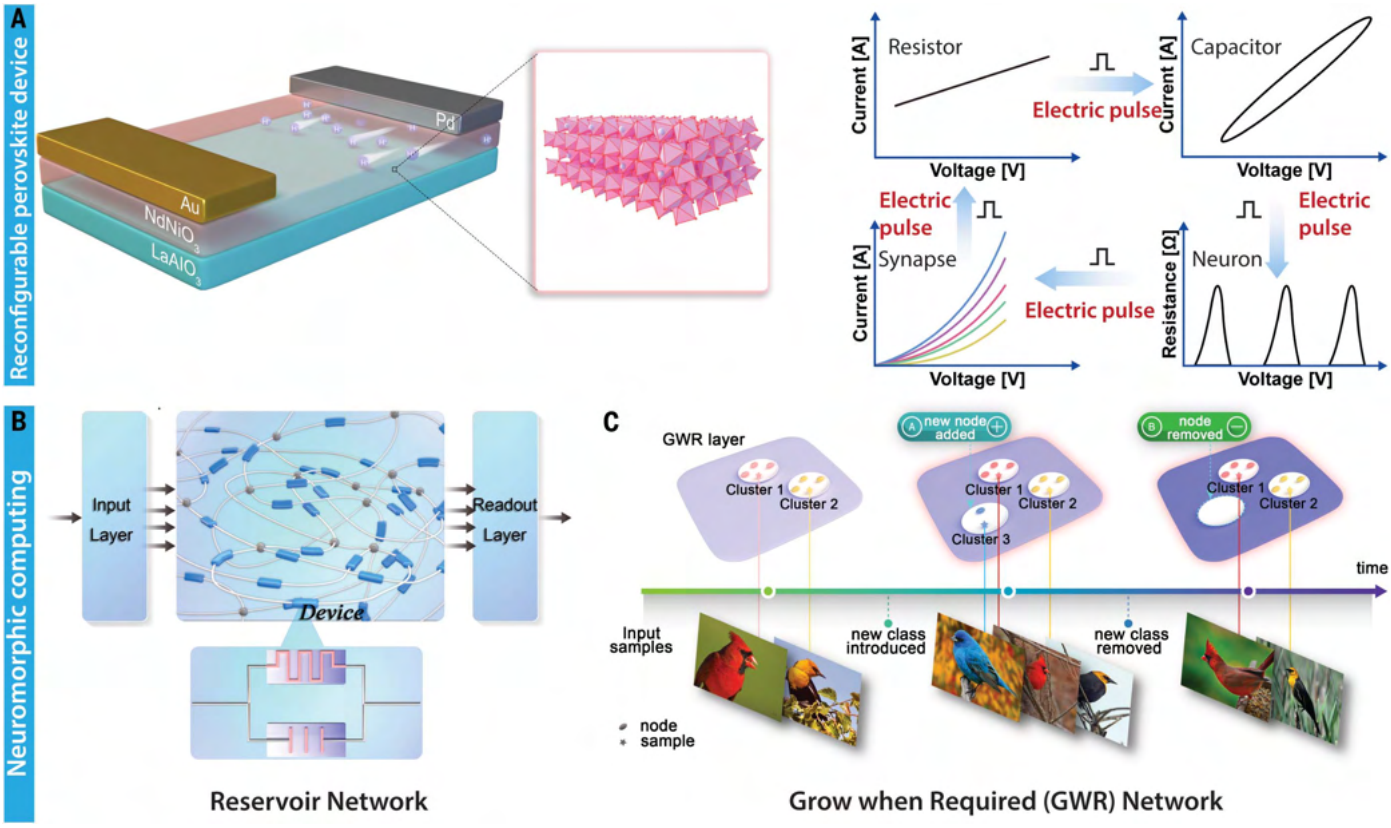

Fig. 1. Reconfigurable perovskite devices. (**A**) Schematic of hydrogen-doped perovskite nickelate as a versatile reconfigurable platform that can be electrically transformed between neurons, synapses, and memory capacitors to enable adaptive neuromorphic computing. By applying electric pulses, the hydrogen ions in the nickelate lattice can occupy metastable states and enable distinct functionalities. (**B**) Schematic of a generic RC framework. An input layer distributes the signals into the reservoir, which projects the inputs into a high-dimensional space. Here, the reservoir is built randomly from programmable devices with memory. No training happens in the reservoir; only the linear readout layer is trained by a simple gradient descent algorithm. The role of the readout layer is to map the high-dimensional dynamics of the reservoir to the output states. (**C**) Schematic of GWR networks. As the network is shown various classes of data, it maps high-dimensional data to a low-dimensional map field to perform clustering on the classes. When a new class is added to the input stream, the network can detect the new input and grow in size by adding network nodes to accommodate it. Additionally, if any of the classes do not appear in the input stream for a long time, the corresponding nodes become inactive, saving resources.

and then eventually saturated at ~10^8 ohms (fig. S5A). Without any hydrogen recharging process to the device for 6 months, hydrogen remained in the NNO lattice, and the resistance of the H-NNO device was stable. To explore the capacitive behaviors of the H-NNO device at different hydrogen doping states, we performed cyclic voltage sweeps (figs. S5, B to H). Pristine and weakly doped perovskite NNO showed linear resistor behavior. At the intermediate doping state, capacitive behavior appears. Electrical reconfiguration of the H-NNO device is summarized in Fig. 2, A to F. By applying positive and negative electric pulses, the resistance state of the device could be modulated carefully, and the programmed resistance states are nonvolatile (fig. S6). At the electronic state i, cyclic voltage sweep measurements of the nickelate device were performed, and linear resistor behavior was observed (Fig. 2A). The electronic state i was then switched to electronic state ii by applying a single voltage pulse, where a current-voltage (*I-V*) loop appeared, indicating stored energy in the device (Fig. 2B). Memristive and memcapacitive behaviors were also demonstrated at state ii (supplementary text 2).

Next, we showed the creation of artificial neurons and synapses (that are responsible for information transfer and memory in the brain) from the same device. Spiking neuronal behavior in the H-NNO device was studied at the electronic state iii (Fig. 2C). Consecutive electric stimuli were applied to the device, and once a critical level was reached, abrupt changes in the device resistance were observed. The nonvolatile neuronal response of the nickelate device to electric stimulus depended on both pulse voltage and pulse width (figs. S7 and S8). A typical spiking probability plot is shown in Fig. 2D, which could be directly implemented in neural networks. We then demonstrated synaptic behavior at electronic state iv in the nickelate device by means of continuous voltage sweeps (Fig. 2E). As sown in fig. S9, threshold pulse fields were investigated for both high-resistance state (HRS; state iii) and low-resistance state (LRS; state iv). At LRS, a smaller threshold pulse field (V_{th}) was sufficient to modulate the device resistance, which was suitable for analog behavior with gradual resistance changes. However, this analog update of device resistance prohibited the sudden jump in resistance necessary for spiking. At HRS, a much higher V_{th} was required to change the resistance and was beneficial for spiking neuronal behavior. Last, the linear resistor state v in Fig. 2F could be restored by applying a single electric pulse. Electrical reconfiguration at various resistance states of the H-NNO device is shown in fig. S10, demonstrating versatility of the device platform. After 1.6×10^6 cycles of endurance measurement of a scaled nickelate device, we performed electrical reconfiguration of the device, and the results showed that all functional modes were reproducible (fig. S11). For example, configuration between linear resistor and capacitor states at initial and after

Downloaded from https://www.science.org at University of Georgia on February 06, 2022

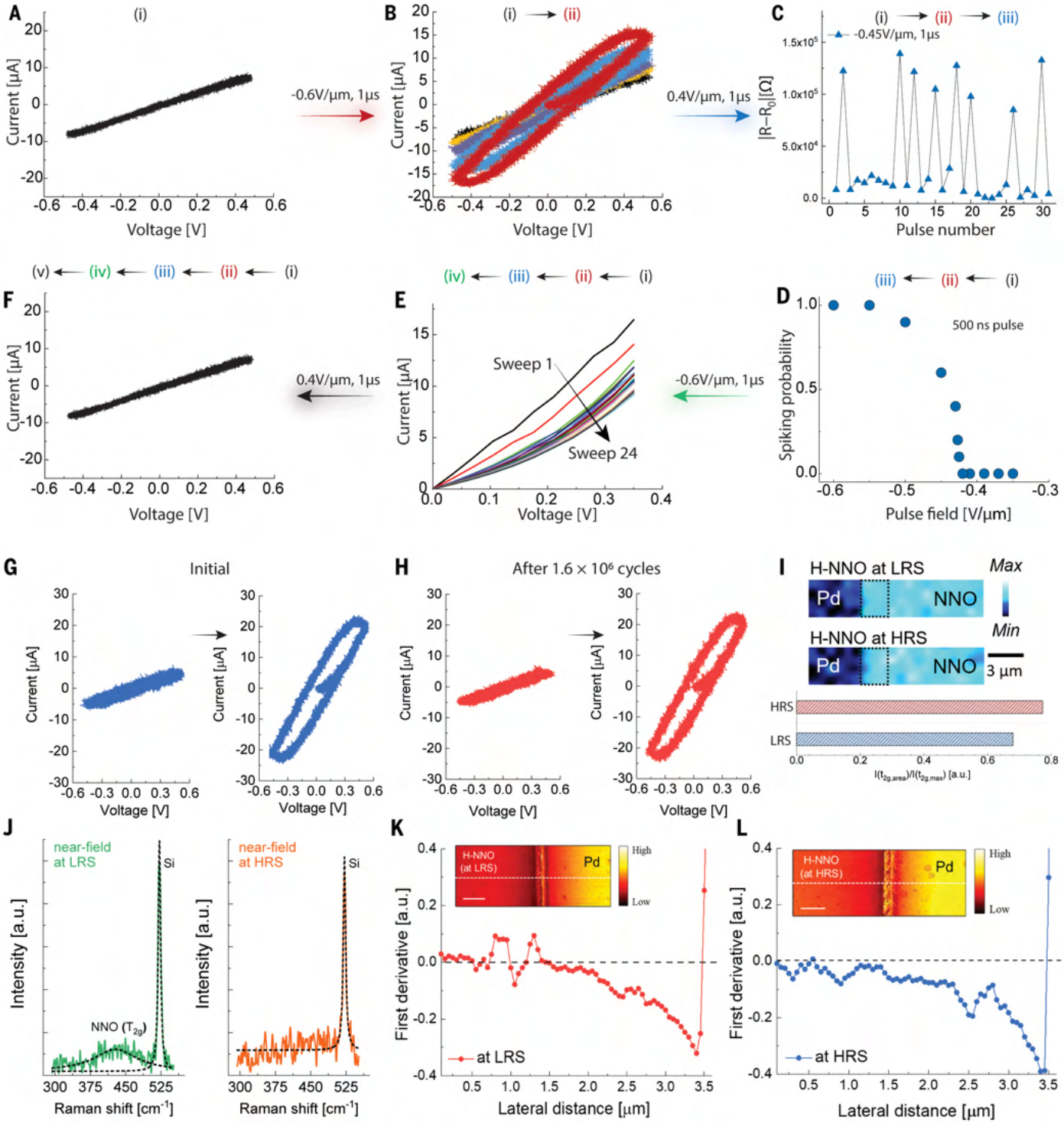

Fig. 2. A single perovskite device can be electrically reconfigured to perform essential functions in a neuromorphic computer. (**A**) Nickelate device as a linear resistor under cyclic voltage sweep. (**B**) Nickelate device as a capacitor under cyclic voltage sweep. The appearance of an *I-V* loop indicates stored energy in the device. *I-V* loops of different sizes can be generated by applying pulse fields (ii). Complete details can be found in supplementary text 2. (**C**) Nickelate device as a spiking neuron (iii). Resistance changes of the nickelate device were monitored in response to consecutive electric pulses (−0.45 V/μm for 1 μs). After the spike fires, the resistance of the device was restored to the original state by applying reset voltage pulse (+0.45 V/μm for 1 μs). (**D**) Spiking probability of nickelate device as a function of pulse field, showing stochastic behavior. (**E**) Nickelate device as a synapse. *I-V* curves of nickelate devices were measured under continuous voltage sweeps. The resistance of the device increases continuously, showing analog synaptic updates. (**F**) Resetting the nickelate device back to initial linear resistor state. (**G** and **H**) Representative electrical reconfiguration between linear resistor and capacitor of the scaled nickelate device at initial and after 1.6×10^6 cycles of endurance measurement. Reconfiguration of all modes are presented in fig. S11. Details of endurance measurement are provided in fig. S22. (**I**) Spatial mapping of Raman (signal to baseline of Raman shift ranging from 320 to

Downloaded from https://www.science.org at University of Georgia on February 06, 2022

470 cm^{-1}) of a 15 by 3 μm^2 rectangular area near the Pd electrode for the H-NNO device at both HRS and LRS. Scale bar, 3 μm. The bright areas correspond to NNO regions in the nickelate device, which showed strong peak intensity of T_{2g} mode at ~439 cm^{-1}. The normalized T_{2g} peak intensity [$I(t_{2g,area})/I(t_{2g,max})$] near the Pd electrode were obtained from the dashed rectangular area. The relative peak intensity of the H-NNO device at LRS was 0.77, whereas that of H-NNO at HRS dropped to 0.68. (**J**) Near-field spectrum (TERS) of H-NNO device at LRS (green) and at HRS (orange), when the Ag tip was engaged near the Pd electrode. The dashed line indicates the fitting of the Raman peak. At LRS of H-NNO, T_{2g} mode was found near the electrode and was suppressed from H-NNO at HRS. (**K** and **L**) Zoom-in of first derivative of the normalized second-harmonic IR near-field amplitude of the H-NNO device at LRS and at HRS near the boundary between the Pd and H-NNO. (Insets) Second-harmonic IR (ω = 952 cm^{-1}) near-field amplitude images of H-NNO devices at LRS and HRS, respectively. Scale bar, 1 μm.

1.6×10^6 cycles of endurance measurement are presented in Fig. 2, G and H, respectively. A single device could be reconfigured as resistor, memcapacitor, neuron, or synapse with electric pulses.

To understand the nanoscale mechanisms that enable electrical reconfiguration, we performed in-depth characterization on representative H-NNO devices at LRS and HRS (Fig. 2, I to L) that correspond to synapse and neuronal states, respectively. Confocal Raman spectra ranging from 300 to 550 cm^{-1} were first collected from two control samples: a pristine NNO film near the Pd electrode and a heavily doped NNO film near the Pd electrode (fig. S12). The T_{2g} mode of NNO was present at ~439 cm^{-1} for pristine NNO, whereas it disappeared for heavily doped NNO, indicating dense proton concentration near the Pd electrode. We performed two-dimensional (2D) Raman mapping (signal to baseline mode, scan range from 320 to 470 cm^{-1}) over a rectangular region (15 by 3 μm^2) at this boundary for the H-NNO device at LRS and at HRS in Fig. 2I. The relative peak intensity of T_{2g} mode of the H-NNO device at LRS was 0.77, whereas for HRS this dropped to 0.68, indicating higher local proton distribution of H-NNO at HRS near the Pd electrode. Near-field tip-enhanced Raman scattering (TERS) was carried on the H-NNO device at LRS and at HRS near the Pd electrode (Fig. 2J). Details of control experiments for near-field TERS are provided in fig. S13. A broad T_{2g} peak of NNO could be seen near the Pd electrode at LRS; however, no such weak peak was detected on NNO near the Pd electrode for H-NNO at HRS, indicating relatively higher proton concentration near the Pd electrode. We used scattering-type scanning near-field optical microscopy (s-SNOM) at a laser frequency of ω = 952 cm^{-1} to image the local distribution of doping of H-NNO devices at LRS and HRS. Details of control experiments for s-SNOM on reference devices are included in fig. S14. Second harmonic infrared (IR) (ω = 952 cm^{-1}) near-field amplitude images of the H-NNO device at LRS and HRS near the Pd electrode are shown in Fig. 2, K and L, insets, respectively. Normalized amplitude line profiles of the NNO devices at LRS and HRS are provided in fig. S15. The first derivative of the normalized amplitude indicates proton concentration changes near the boundary between the Pd electrode and H-NNO channel shown in Fig. 2, K and L. At HRS, the proton concentration changed over a longer lateral distance compared with that of at LRS. The s-SNOM amplitude signal differences revealed local chemical composition differences in H-NNO at different functional states, which was consistent with Raman results. Further, the carrier localization length scale of H-NNO device at HRS was smaller than that at LRS, as determined from temperature-dependent electrical transport measurements (fig. S16). The nanoscale chacterization of devices showed consistent results that the local proton distribution of H-NNO device at LRS and HRS near the Pd electrode were different. Density functional theory (DFT) calculations further indicated that differences in the location of protons could lead to modulation of energy band gap of NNO (figs. S17 to S20), which is of relevance to different functional states. Nudged elastic band (NEB) calculations showed that the proton migration barrier could vary from 0.2 to 0.6 eV, depending on the migration path (supplementary text 1). Therefore, different local proton distributions at LRS and at HRS of the H-NNO device could lead to different functional states.

We also fabricated nickelate devices with 100 nm gap size to demonstrate scalability, endurance, reproducibility, and ultralow energy consumption (figs. S21 to S24). In scaled devices, electrical reconfiguration could be realized with <10-ns electric pulses. The energy cost for a single synaptic update was ~2 fJ, which is comparable with that in the brain (1 to ~100 fJ) (*12*). To demonstrate compatibility with CMOS (complementary metal-oxide semiconductor) technology, nickelate devices were fabricated on SiO_2 on Si substrates through both sputtering and ALD (an industrial technique used to grow high-quality metal-oxide films for state-of-the-art electronics), and data are shown in figs. S25 and S26.

To showcase applications of the adaptive nickelate hardware, we applied the experimental memristive and memcapacitive behaviors in RC, a brain-inspired machine-learning architecture that addresses the issue of training complexity and parameter explosion, commonly observed in traditional recurrent neural networks (RNNs), by only adapting a simple output layer. RC explains higher-order cognitive functions and the interaction of short-term memory with other cognitive processes (*13*). Details can be found in supplementary text 2. To have a baseline comparison, we evaluated the performance of our H-NNO device in comparison with theoretical models (*14*, *15*) and experimental reports (*16*, *17*) for three different tasks: MNIST (Modified National Institute of Standards and Technology database) digit recognition, isolated spoken digit recognition, and ventricular heartbeat classification on an electrocardiogram (ECG) dataset. The simulation results in Fig. 3, A to C, demonstrate that our H-NNO reservoirs could achieve comparable performances on the three tasks with fewer devices compared with the theoretical and experimental reservoirs. The results of performance-device ratios in Fig. 3D show that our H-NNO reservoirs, on average, outperformed the theoretical and experimental reservoirs by a factor of 1.4×, 1.2×, and 5.1× for MNIST, isolated spoken digits, and ECG heartbeat, respectively. Detailed explanations of the performance are in supplementary text 2.

Having the neuronal and synaptic functionality in a single type of device could enable compact and energy-efficient neuromorphic system designs. Discussion on deep neural networks that use such perovskite networks is given in supplementary text 3. Furthermore, the ability to reconfigure devices for multiple neuromorphic functions opens up their innovative use in next-generation AI—namely, in the emerging domain of dynamic neural networks. The GWR network is one such example that creates new nodes and their interconnections according to competitive Hebbian learning. The GWR networks expand on the concept of self-organizing neural networks by adding or removing network nodes in an unsupervised manner to approximate the input space accurately and at times more parsimoniously as compared with a static self-organizing map (*18*). We can compare the dynamic GWR with a static self-organizing network that uses the same Hebbian learning scheme but has a fixed number of nodes, initialized randomly in the beginning. We trained our network on two archetypal datasets used to evaluate performance in literature, MNIST (*19*) and a subset of CUB-200 (*20*), to simulate how such a network will perform on the fly.

Downloaded from https://www.science.org at University of Georgia on February 06, 2022

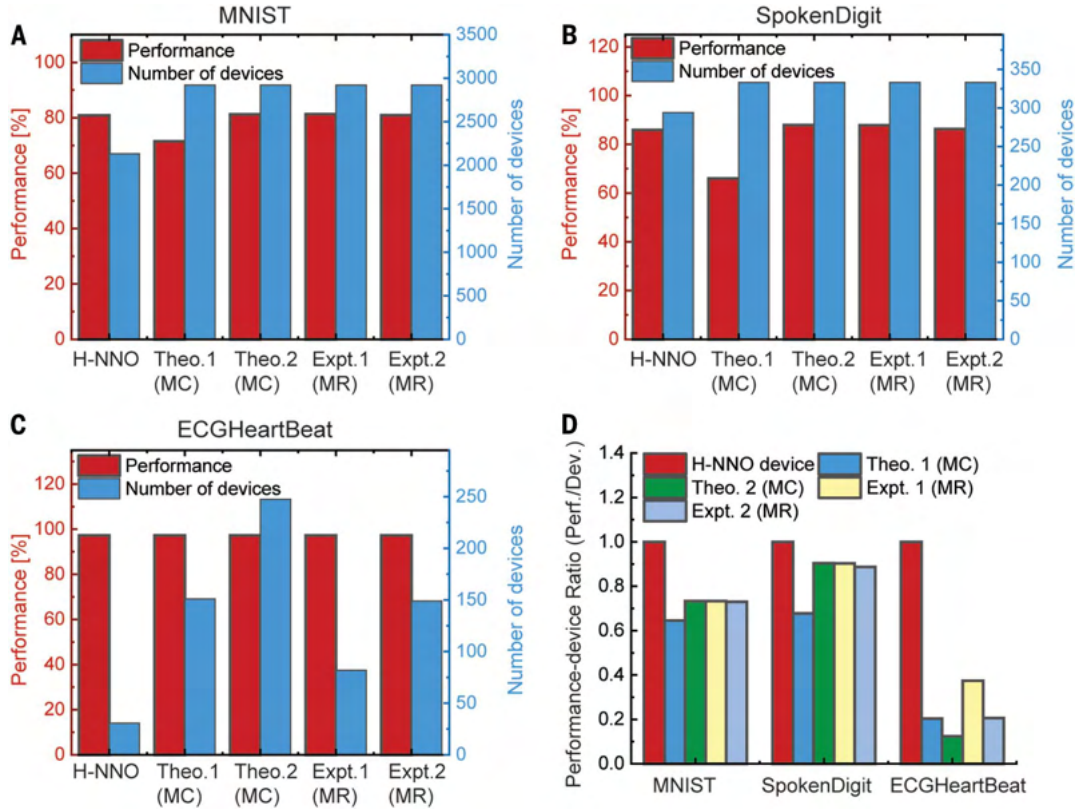

Fig. 3. Reservoir computing simulations with data measured from nickelate devices. (**A** to **D**) The simulation results of reservoirs with H-NNO devices, compared with theoretical and experimental memristive models of reservoirs, demonstrated that a large and random network of H-NNO devices could function as a hardware platform for neuromorphic computing in solving complex tasks. The simulation results were based on the average results of simulating a sample size of 100 reservoirs with similar hyperparameters for each reservoir type to reduce uncertainty owing to the stochastic nature of reservoir networks. As shown in (A) to (C), the H-NNO reservoirs could achieve comparable performances on three tasks with fewer devices. The performance/device ratios in (D) indicate that the H-NNO reservoirs, on average, outperformed the theoretical and memristive reservoirs by a factor of 1.4×, 1.2×, and 5.1× for MNIST, isolated spoken digits, and ECG heartbeats, respectively.

Discussion on the datasets and details of the simulation are available in the supplementary materials, materials and methods, and supplementary text 4. The GWR network's ability to dynamically respond to changes in the input distribution is visualized in Fig. 4A for MNIST.

For both the datasets and networks, we conducted two sets of simulations using the experimental data from our H-NNO devices: (i) incremental learning, in which the network is shown newer classes of data over time, and (ii) assessing the effect of growing or shrinking compared with static networks—how efficiently the GWR can represent the input space. The network's test accuracy and the number of nodes as each new class was trained for both the datasets in the incremental learning scenario are shown in Fig. 4, B to E. We observed that the dynamic network was able to retain its learned representations much better than could the static network, with the final test of accuracy resulting in MNIST being 212% more accurate and CUB-200 being 250% more accurate. By growing its size, the network avoided suffering from catastrophic forgetting and showed only a smooth degradation in performance as the number of classes was increased. The size of the static network was chosen to be equal to the maximum number of nodes that the GWR network required. This arrangement ensured that the difference we observed was not due to the size difference of the two networks but rather because of the dynamic network's ability to grow and learn.

We then studied the ability of the GWR network to dynamically change its size to adapt to the input space. First, we assessed the networks' ability to grow as the number of classes in the network was increased abruptly (Fig. 4, F and G). Initially, we presented the networks with the first half of the total number of classes in the datasets, and the GWR grew and saturated in size. Afterward, when the networks were presented with the entire dataset, the GWR rapidly grew its size to accommodate the change. The static network was not able to do so and thus failed to learn the new data, also suffering degradation in performance in the initial classes (detailed accuracy results are provided in supplementary text 4 and figs. S27 and S28). Overall, the dynamic networks achieved better accuracy on the test set in comparison with that of the static network: 210% for MNIST and 170% for CUB-200. Next, we demonstrated that the GWR was able to efficiently allocate its resources compared with a large static network. We presented the network with all the classes of the dataset at the beginning. After learning occurred, we removed half the categories and let the GWR network reduce its size and reach an equilibrium number of nodes (Fig. 4, H and I). We found that the GWR was able to retain a similar level of the performance to that of the large static network (accuracy difference, 2 to 3%) on the subset of interest and demonstrated higher efficiency through shrinking its size by ~47% for MNIST and ~27% for CUB-200 (detailed accuracy results are provided in supplementary text 4 and figs. S29 and S30) In addition to simulation studies, we conducted proof-of-concept experiments to demonstrate the reconfiguration ability of the H-NNO devices in hardware for an incremental learning scenario, in comparison with a static network. Detailed discussions on the results are included in supplementary text 5.

Conclusions

We have demonstrated artificial neurogenesis in perovskite electronic devices: the ability to reconfigure hardware building blocks for brain-inspired computers on demand within a single device platform. Dynamic deep learning networks simulated with the experimentally measured characteristics of the nickelate devices consistently outperformed static counterparts. The results showcase the potential of reconfigurable perovskite quantum electronic devices for emerging computing paradigms and AI machines. Additionally, semiconductor technology–compatible ALD on Si platforms

Downloaded from https://www.science.org at University of Georgia on February 06, 2022

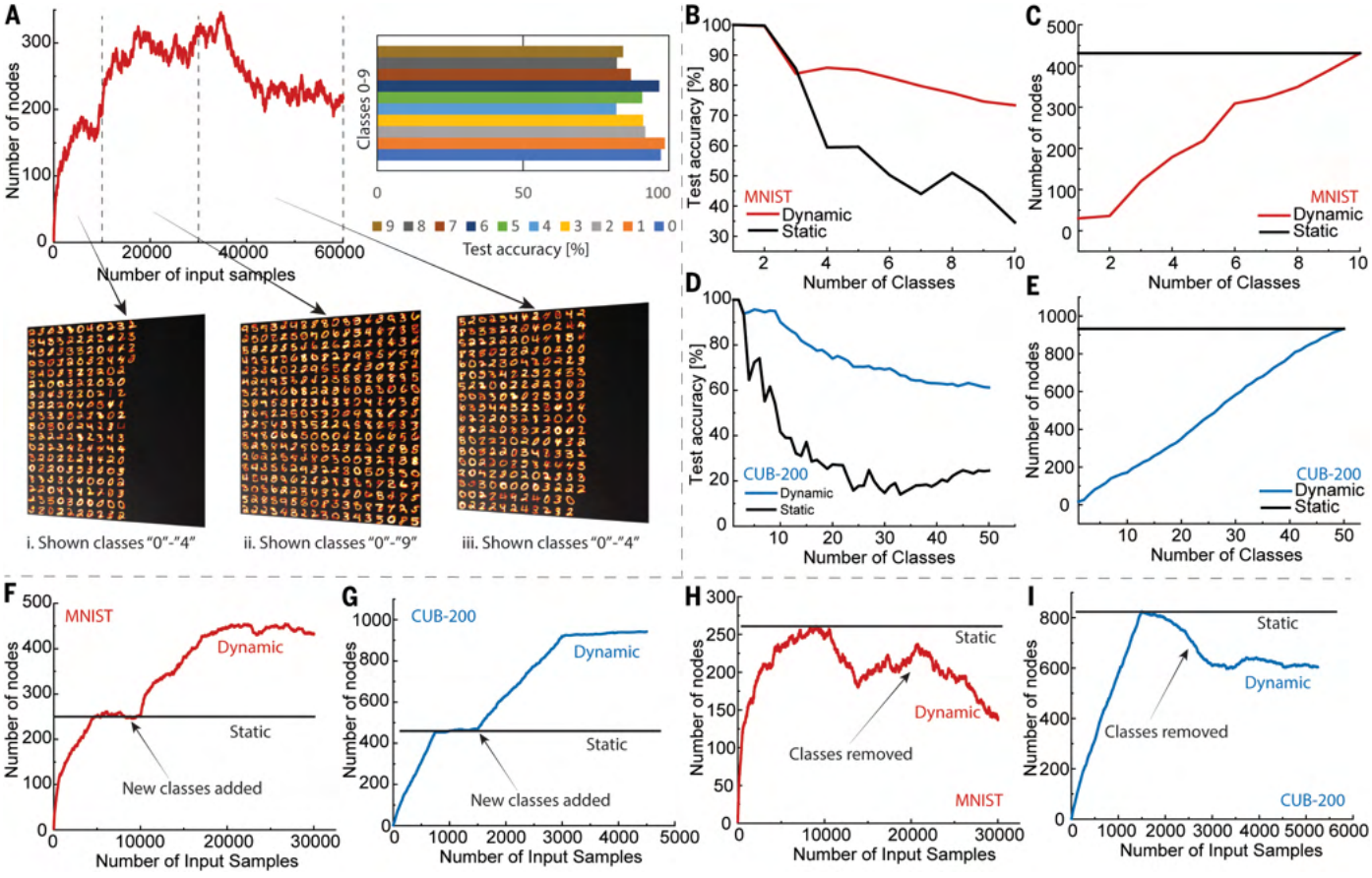

Fig. 4. Dynamic grow-when-required computing with experimental characteristics measured from nickelate devices. (**A**) Visualization of the GWR network's ability to dynamically respond to changes in the input distribution over time for the MNIST dataset. First, we showed the network 10,000 input samples from the first five classes ("0" to "4") of the MNIST dataset. The network could grow and learn the representation as seen in i. Next, the network was trained on 20,000 samples from all the 10 classes of the MNIST. Because of the addition of new classes, the network grew in size and accommodated them, as seen in ii. The accuracy over all the classes is shown in the bar chart (top right). Last, we again changed the input class distribution by only showing the network the classes "0" to "4". We observed that the network could gradually shrink its size as nodes associated with the last five classes slowly became inactive and were removed from the network, as seen in iii. Here, the digits are the learned representations of the nodes, whereas each unit of the black region indicates an unused and inactive node in the network. (**B** to **E**) Network performance for incremental learning of classes. (B) Test accuracy for MNIST as the number of classes is incrementally increased from 1 to 10. (C) Number of nodes as the number of classes is increased for MNIST. (D) Test accuracy for the 50 classes of CUB-200 as the number of classes is incrementally increased from 1 to 50. (E) Number of nodes as the number of classes is increased for CUB-200. (**F** to **I**) Assessing the effect of dynamically changing size of GWR compared with static network with fixed number of nodes. [(F) and (G)] The GWRs achieved 51.6% better accuracy on MNIST and 41.3% better accuracy on CUB-200 as compared with static networks that were not allowed to grow beyond the size of the dynamic network before learning the new classes. [(H) and (I)] We observed similar performance on the classes that are available in both the networks; however, the dynamic network achieves these results with almost half (~47.3%) the number of resources and nodes for MNIST and ~27% fewer nodes for the 50 classes of CUB-200 compared with the static networks.

and room-temperature operation of test chips can further enable widespread adoption of perovskite quantum materials into mainstream integrated circuit manufacturing.

REFERENCES AND NOTES

1. J. Kirkpatrick *et al.*, *Proc. Natl. Acad. Sci. U.S.A.* **114**, 3521–3526 (2017).
2. G. I. Parisi, R. Kemker, J. L. Part, C. Kanan, S. Wermter, *Neural Netw.* **113**, 54–71 (2019).
3. G. I. Parisi, X. Ji, S. Wermter, On the role of neurogenesis in overcoming catastrophic forgetting, from NIPS'18 Workshop on Continual Learning, Monteral, Canada, 7 December 2018.
4. K. O. Stanley, J. Clune, J. Lehman, R. Miikkulainen, *Nat. Mach. Intell.* **1**, 24–35 (2019).
5. N. K. Upadhyay *et al.*, *Adv. Mater. Technol.* **4**, 1800589 (2019).
6. T. Ohno *et al.*, *Nat. Mater.* **10**, 591–595 (2011).
7. R. A. John *et al.*, *Adv. Mater.* **30**, e1800220 (2018).
8. R. A. John *et al.*, *Nat. Commun.* **11**, 3211 (2020).
9. W. Yi *et al.*, *Nat. Commun.* **9**, 4661 (2018).
10. J. H. Yoon *et al.*, *Nat. Commun.* **9**, 417 (2018).
11. J. Shi, Y. Zhou, S. Ramanathan, *Nat. Commun.* **5**, 4860 (2014).
12. Y. van de Burgt *et al.*, *Nat. Mater.* **16**, 414–418 (2017).
13. M. Rigotti, D. Ben Dayan Rubin, X.-J. Wang, S. Fusi, *Front. Comput. Neurosci.* **4**, 24 (2010).
14. M. G. A. Mohamed, H. Kim, T. W. Cho, *ScientificWorldJournal* **2015**, 910126 (2015).
15. D. Biolek, M. Di Ventra, Y. V. Pershin, *Wuxiandian Gongcheng* **22**, 945–968 (2013).
16. S. H. Jo *et al.*, *Nano Lett.* **10**, 1297–1301 (2010).
17. A. S. Oblea, A. Timilsina, D. Moore, K. A. Campbell, Silver chalcogenide based memristor devices, in *The 2010 International Joint Conference on Neural Networks (IJCNN)* (IEEE, 2010), pp. 1–3.
18. S. Marsland, J. Shapiro, U. Nehmzow, *Neural Netw.* **15**, 1041–1058 (2002).
19. Y. LeCun, L. Bottou, Y. Bengio, P. Haffner, *Proc. IEEE.* **86**, 2278–2324 (1998).
20. C. Wah, S. Branson, P. Welinder, P. Perona, S. Belongie, The Caltech-UCSD Birds-200-2011 Dataset, *Comput. Neural Syst. Tech. Rep.* CNS-TR-2011-001 (California Institute of Technology, 2011).
21. H.-T. Zhang *et al.*, Data from reconfigurable perovskite nickelate electronics for artificial intelligence, *Zenodo* (2021).

ACKNOWLEDGMENTS

We sincerely thank A. Chubykin at the Purdue Institute for Integrative Neuroscience for valuable discussions on neurogenesis, synaptogenesis, and repair of neural circuits. We sincerely thank K. Rabe (Rutgers University), S. Mandal (Rutgers University),

Downloaded from https://www.science.org at University of Georgia on February 06, 2022

and M. Kotiuga (EPFL) for valuable discussions on mechanisms leading to capacitive behavior in hydrogen-doped nickelates. We thank A. Hexemer for providing us computational time on NERSC and useful discussions on the workflow development for predicting the metastable phases of materials. **Funding:** The analysis of the synaptic properties and related measurements were supported by Quantum Materials for Energy Efficient Neuromorphic Computing (Q-MEEN-C), an Energy Frontier Research Center (EFRC) funded by the US Department of Energy (DOE), Office of Science, Basic Energy Sciences (BES), under award DE-SC0019273. The fabrication and pulsed field measurements were supported by the Air Force Office of Scientific Research (AFOSR) FA9550-19-1-0351 and ARO W911NF-19-2-0237, respectively. A.N.M.N.I. and A.S.'s research was funded in part by the National Science Foundation (NSF) under grants BCS-2031632 and CCF-1955815. Use of the Center for Nanoscale Materials and Advanced Photon Source, both Office of Science user facilities, was supported by the DOE, Office of Science, BES, under contract DE-AC02-06CH11357. This research used resources of the National Energy Research Scientific Computing Center (NERSC), a DOE Office of Science User Facility located at Lawrence Berkeley National Laboratory, operated under contract DE-AC02-05CH11231. This material is based on work supported by the DOE, Office of Science, BES Data, Artificial Intelligence and Machine Learning at DOE Scientific User Facilities program. This work at BNL was supported by DOE-BES, Materials Sciences and Engineering Division under contract DE-SC0012704. This research used resources of the Advanced Photon Source, a DOE Office of Science User Facility, operated for the DOE Office of Science by Argonne National Laboratory under contract DE-AC02-06CH11357. Extraordinary facility operations were supported in part by the DOE Office of Science through the National Virtual Biotechnology Laboratory, a consortium of DOE national laboratories focused on the response to COVID-19, with funding provided by the Coronavirus CARES Act. S.G. and Y.A. acknowledge support from the AFOSR, grant FA9559-16-1-0172, and NSF under grant DMR-1904097. S.M. and N.J. acknowledge support from NSF grant CHE-1944796. **Author contributions:** H.-T.Z., T.J.P., and S.R. conceived the study. T.J.P. and H.-T.Z. grew the nickelate films. Q.W. fabricated the devices. H.-T.Z., T.J.P., and S. Mo. conducted electrical measurements. H.Y. and T.J.P. performed XRD characterization. H.Z. performed synchrotron x-ray characterization. S.C. and Y.Z. performed transmission electron microscopy (TEM) characterization. S.G. and Y.A. carried out scattering-type scanning near-field optical microscopy. S. Mah. and N.J. performed near-field tip-enhanced Raman measurements. A.N.M.N.I. and A.S. performed the all-perovskite deep network and the GWR neural network simulations and analysis. D.S.J.T. performed the RC simulation, and C.T. co-led the discussions of these results. S. Man., S.B., and S.K.R.S.S. carried out all the reinforcement learning–based search and the ab initio calculations. H.-T.Z., T.J.P., and S.R. organized the manuscript. All authors participated in discussing the results and providing various sections and comments for the paper. **Competing interests:** The authors declare no competing interests. **Data and materials availability:** All data needed to evaluate the conclusions in the paper are present in the paper or the supplementary materials. Data can be found at the Zenodo repository (*21*).

SUPPLEMENTARY MATERIALS

science.org/doi/10.1126/science.abj7943
Materials and Methods
Supplementary Text
Figs. S1 to S55
Tables S1 to S4
References (*22*–*58*)

2 June 2021; resubmitted 19 November 2021
Accepted 13 December 2021
10.1126/science.abj7943

Downloaded from https://www.science.org at University of Georgia on February 06, 2022

Science

Reconfigurable perovskite nickelate electronics for artificial intelligence

Hai-Tian ZhangTae Joon ParkA. N. M. Nafiul IslamDat S. J. TranSukriti MannaQi WangSandip MondalHaoming YuSuvo BanikShaobo ChengHua ZhouSampath GamageSayantan MahapatraYimei ZhuYohannes AbateNan JiangSubramanian K. R. S. SankaranarayananAbhronil SenguptaChristof TeuscherShriram Ramanathan

Science, 375 (6580), • DOI: 10.1126/science.abj7943

Reconfigurable neuromorphic functions

Having all the core functionality required for neuromorphic computing in one type of a device could offer dramatic improvements to emerging computing architectures and brain-inspired hardware for artificial intelligence. Zhang *et al*. showed that proton-doped perovskite neodymium nickelate (NdNiO) could be reconfigured at room temperature by simple electrical pulses to generate the different functions of neuron, synapse, resistor, and capacitor (see the Perspective by John). The authors designed a prototype experimental network that not only demonstrated electrical reconfiguration of the device, but also showed that such dynamic networks enabled a better approximation of the dataset for incremental learning scenarios compared with static networks. —YS

View the article online
https://www.science.org/doi/10.1126/science.abj7943
Permissions
https://www.science.org/help/reprints-and-permissions

Downloaded from https://www.science.org at University of Georgia on February 06, 2022

Use of think article is subject to the Terms of service

Science (ISSN) is published by the American Association for the Advancement of Science. 1200 New York Avenue NW, Washington, DC 20005. The title *Science* is a registered trademark of AAAS.
Copyright © 2022 The Authors, some rights reserved; exclusive licensee American Association for the Advancement of Science. No claim to original U.S. Government Works